Proceedings of ASME Turbo Expo 2011
GT2011
June 6-10, 2011, Vancouver, British Columbia, Canada

GT2011-45624

THEORY AND APPLICATION OF AXISYMMETRIC ENDWALL CONTOURING FOR COMPRESSORS

Georg Kröger, Christian Voß and Eberhard Nicke
German Aerospace Center
Institute of Propulsion Technology
Fan and Compressor Department
51147 Cologne, Germany
georg.kroeger@dlr.de christian.voß@dlr.de eberhard.nicke@dlr.de

Christian Cornelius
Siemens AG
Fossil Power Generation Division
Mellinghofer Str. 55
45473 Mühlheim an der Ruhr, Germany
christian.cornelius@siemens.com

ABSTRACT

Engine operating range and efficiency are of increasing importance in modern compressor design for heavy duty gas turbines and aircraft engines. These highly challenging objectives can only be met if all components provide high aerodynamic performance and stability. The aerodynamic losses of highly loaded axial compressors are mainly influenced by the leakage flow through clearance gaps. Especially the leakage flow due to the radial clearances of rotor blades affects negatively both, the efficiency and the operating range of the engine.

Recent publications showed that the clearance flow and the clearance vortex can be influenced by an additional static pressure gradient at the outer casing, which is created by an axisymmetric wavy casing shape. A notable performance increase of up to 0.4% stage efficiency at design point conditions was reported for high pressure stages with large tip clearance heights [1] as well as for a transonic stage with a relatively small radial clearance gap [2].

An analytic approach to predict the effects of axisymmetric casing contouring has been developed at DLR, Institute of Propulsion Technology, and is outlined in the first part of this work. The characteristic behavior of the clearance vortex in an adverse pressure gradient is discussed by means of an inviscid vortex model [3]. The critical vortex parameters are isolated and related to the static pressure increase due to the casing contour.

The second part illustrates the application of an axisymmetric endwall contour. A three dimensional optimization of the outer casing and the corresponding blade tip airfoil section of a typical gas turbine high pressure compressor stage with a high number of free variables is presented. The optimization led to a significant increase in aerodynamic performance of about 0.8% stage efficiency and to a notable reduction of the endwall blockage at ADP conditions. Furthermore, an improved off-design performance was found and a simple design rule is given to transfer both, the casing contour and the blade tip section modification on similar high pressure compressor blades.

Based on these design rules the results of the optimized stages were applied to the rear stages of a Siemens gas turbine compressor CFD model. An increase of 0.3% full compressor performance was reached at design point conditions.

NOMENCLATURE

Abbreviations

ADP	Aerodynamic Design Point
CFD	Computational Fluid Dynamics
DLR	German Aerospace Center
HP	High Pressure
HPA	High Performance Airfoil
PS	Pressure Side
SS	Suction Side

Greek Symbols

β	Prandtl factor: $\sqrt{1-M_\infty^2}$ [-]
η	Dynamic viscosity [Pa·s]
Γ	Circulation [m]

ω	Angular velocity [1/s]
φ	Perturbation potential $[m^2/s]$

Fluidmechanical Symbols

$\vec{V}$	Velocity vector [m/s]
A_0	Wave amplitude [m]
A_z	Wave amplitude [m]
c_p	Pressure coefficient [-]
m/M	Relative massflow [-]
M_∞	Reference Mach number [-]
p_{far}	Static farfield pressure [Pa]
S_c	Maximum swirl ratio [-]
S_{ci}	Initial swirl ratio [-]
S_{crit}	Critical swirl ratio [-]
u_θ	Pitch-wise velocity [m/s]
u_x	Axial velocity [m/s]
A	Vortex core cross sectional area $[m^2]$
a	Vortex core radius [m]
b	Wall distance [m]
D	Critical vortex parameter [-]
L	Power [W]
l	Wave length [m]
p	Static pressure [Pa]
r	Radius [m]
t	Clearance height [m]
u	Axial velocity [m/s]

INTRODUCTION

The operational mode of modern gas turbine power plants is nowadays primarily focused on two competing states, base load and peak load operation. Whilst the base load operational mode demands maximal thermodynamic efficiency and component performance combined with a high, steady power output, the peak load operation mode mainly gives prominence to a very fast engine start up capability and a wide operating range. Especially at peak operation, an engine hot restart event is common determining the critical size of the radial clearance gaps in the subsonic high pressure compressor stages. Since the efficiency and the operating range of the compressor are essentially related to the clearance flow losses, their reduction makes an important contribution to the overall efficiency and stability improvement.

Clearance flow losses can be efficiently decreased by means of axisymmetric endwall contouring, see figure 1. This approach was firstly reported for rotors of high pressure stages by Kröger et al. [1, 4] and enhanced to transonic rotors [2].

In addition to the publications mentioned, the following work highlights in the first part an analytical approach to understand and to predict the effects of axisymmetric casing contours. The characteristics of the clearance flow are discussed and an inviscid vortex model is used to assess the effect of an adverse pressure gradient on the clearance vortex. Furthermore,

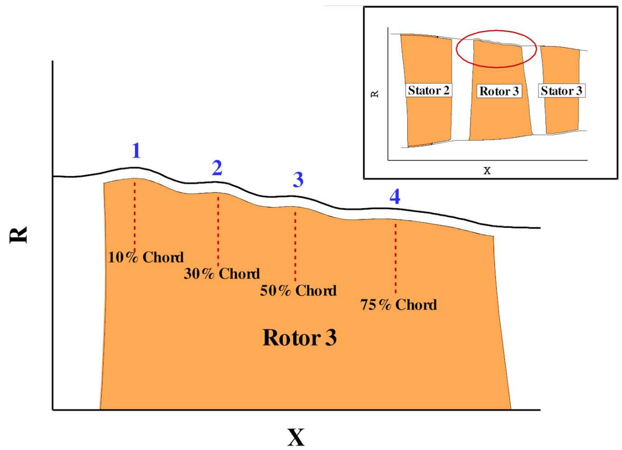

FIGURE 1. AXISYMMETRIC ENDWALL CONTOUR FOR A TRANSONIC ROTOR [2]

the static pressure increase due to the casing contour is quantified.

The second part is focused on the industrial application of the axisymmetric casing contouring. A multiobjective optimization of the outer casing annulus line and the blade tip airfoil section of a typical high pressure compressor stage with 38 free variables is presented to render the improvement potential of an isolated single stage at ADP conditions. A simple design rule is developed to transfer the optimized blade tip airfoil section and the casing contour to other high pressure compressor blades. Finally, the design rule is applied to the rear stages of a Siemens gas turbine compressor and evaluated by means of a steady state, single passage full compressor CFD simulation.

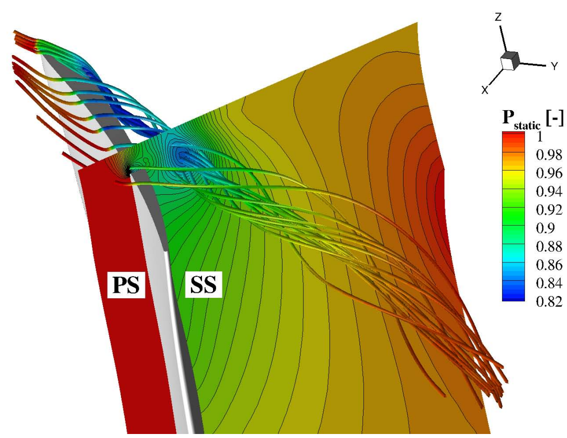

FIGURE 2. CLEARANCE FLOW AND CLEARANCE VORTEX OF A TYPICAL HIGH PRESSURE COMPRESSOR BLADE, STATIC PRESSURE NORMALIZED WITH MAXIMUM STATIC PRESSURE WITHIN THE FLOW FIELD [5]

GENERAL CLEARANCE FLOW CHARACTERISTICS

As illustrated in figure 2 the clearance flow can be subdivided into two main phases: The flow in the clearance gap and the mixing process of the leakage flow with the main flow. While entering the clearance gap on the pressure side (PS) of the blade, the clearance flow is accelerated around the edge of the blade and a sudden decrease of the static pressure is observed. The flow is forced to separate from the blade tip close to the PS of the blade reducing the effective flow area in the clearance gap. The flow in the clearance gap is accelerated further to the suction side (SS) of the blade close to the leading edge and rolls up into the stable clearance vortex. The formation of the clearance vortex essentially affects the static pressure distribution of the SS of the blade close to the clearance gap [1, 6]. The clearance vortex separates from blade SS in the area of the minimum static pressure and develops to the PS of the adjacent blade and in radial direction downwards. Speaking generally, the governing parameters for the leakage flow and the clearance vortex are:

- the clearance height
- the overall blade loading
- the airfoil section at the blade tip
- the static pressure distribution near the casing [1, 2]

The clearance vortex is commonly approximated as Rankine vortex **[7, 9]** and thus the vortex core is assumed to rotate around the rotational-axis as a solid body with radius a and constant angular velocity ω yielding the following velocity distribution in $(x, r, \theta) - coordinates$ (see figure 6):

$$\begin{array}{l} u_\theta = \omega r \quad u_x = u_x(r) \quad r \leq a \\ u_\theta = \frac{\omega a^2}{r} \quad u_x = const. \ r > a \end{array} \tag{1}$$

Another dimensionless parameter to characterize the vortex strength is the maximum swirl ratio of the vortex core S_c defined in terms of the core velocity components and the core radius:

$$S_c = \frac{u_{\theta max}}{u_x} \tag{2}$$

Kang and Hirsch [7] report in their cascade experiments maximum swirl ratios of about 0.35 in early stages of the vortex development and Smart et al. [8] state a value of about 0.32. For the given industrial application of a high pressure stage gas turbine rotor, a swirl ratio of 0.27 has been evaluated numerically [5].

To predict the behavior of a Rankine vortex in an adverse pressure gradient Darmofal et al. [9] developed a simple but very useful inviscid model for a Rankine vortex which is mainly based on the radial equilibrium in the vortex core and the conservation of mass and momentum. As a result a critical parameter D for the vortex core behavior is defined in analogy to the *Mach* number in compressible flows. D is a function of the maximum swirl ratio S_c:

$$D = \frac{\sqrt{2}}{S_c} \tag{3}$$

Consequently, if $D > 1$ ($S_c < \sqrt{2}$) the vortex core state is called super-critical and if $D < 1$ ($S_c > \sqrt{2}$) the flow is referred to as sub-critical. According to this, critical conditions for the vortex core occur at $D = 1$ at the critical maximum swirl ratio $S_{crit} = \sqrt{2}$. The vortex core suffers from a large expansion and instability when reaching the critical value of $D = 1$ [3, 9].

The response of the vortex to an adverse static pressure gradient in the far field ($\Delta p_{far} > 0$ in direction of the vortex propagation) is discussed in the publication of Darmofal et al. [9] and resumed in Greitzer et al. [3]. Two major conclusions can be drawn:

- Sub-critical vortices increase their axial velocity in the core and thus reduce their core cross sectional area A in the presence of an adverse pressure gradient $\frac{dA}{dp_{far}} < 0$.
- Super-critical vortices decrease their axial velocity in the core and thus increase their core cross sectional area A in the presence of an adverse pressure gradient $\frac{dA}{dp_{far}} > 0$.

Since the axial velocity and the core cross sectional area changes due to the static pressure gradient the local swirl ratio S_c changes as well. As mentioned before, a sudden vortex core extension takes place if the critical swirl ratio $S_{crit} = \sqrt{2}$ is reached. Hence, the critical static far field pressure increase to reach the critical swirl ratio can be expressed in terms of the initial (local) swirl ratio of the vortex core S_{ci} (see [3, 9] for derivation):

$$\left(\frac{\Delta p_{far}}{\frac{1}{2}\rho u_{xi}^2} \right)^* = 1 - S_{ci}^2 + \frac{S_{ci}^4}{4} \tag{4}$$

PRESSURE GRADIENT DUE TO CASING CONTOURING

The variation of the static pressure close to the casing contour can be approximated quantitatively by means of a linearized two-dimensional compressible inviscid subsonic flow along a sinusoidal endwall. The problem is presented in figure 3. Since the amplitude $A_0 \ll l$ and the flow along the endwall is subsonic the problem can be regarded as linear.

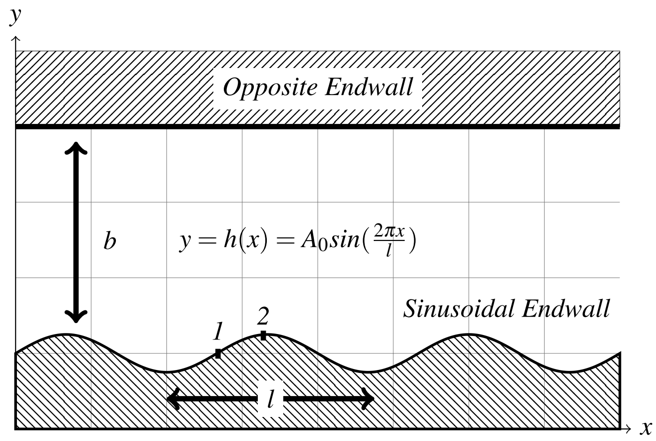

FIGURE 3. FLOW ALONG A SINUSOIDAL ENDWALL, Burg et al. [10]

Starting from the compressible linearized two-dimensional perturbation potential equation

$$(1 - M_\infty{}^2)\,\varphi_{xx} + \varphi_{yy} = 0 \tag{5}$$

Burg et al. [10] give the analytic solution for a given sinusoidal endwall ($y = h(x) = A_0 \cdot sin(\frac{2\pi x}{l})$) upon the discussed assumptions for a subsonic flow with a infinite distance b of the opposite endwall:

$$\frac{\varphi_x(x,y)}{u_\infty} = \frac{u - u_\infty}{u_\infty} = \frac{A_0}{\beta}\frac{2\pi}{l} sin\left(2\pi\frac{x}{l}\right) \cdot e^{-2\pi\beta\frac{y}{l}} \tag{6}$$

In equation 6, $\beta = \sqrt{1 - M_\infty^2}$ is the Prandtl factor, u is the axial velocity and φ_x is the perturbation velocity. Zierep [11] presents the relationship between the perturbation velocity φ_x and the static pressure coefficient c_p for small perturbations:

$$c_p := \frac{p - p_\infty}{\frac{1}{2}\rho_\infty u_\infty^2} \simeq -2 \cdot \frac{u - u_\infty}{u_\infty} = -2 \cdot \frac{A_0}{\beta}\frac{2\pi}{l} sin\left(2\pi\frac{x}{l}\right) \cdot e^{-2\pi\beta\frac{y}{l}} \tag{7}$$

Following equation 7, the static pressure raise of the casing contour between the positions $2 : \frac{x}{l} = \frac{1}{4}$ and $1 : \frac{x}{l} = 0$ can be calculated as (sign changed because the flow is underneath the endwall):

$$c_{p2} - c_{p1} = \frac{p_2 - p_1}{\frac{1}{2}\rho_\infty u_\infty^2} = \frac{\Delta p_{21}}{\frac{1}{2}\rho_\infty u_\infty^2} = 4 \cdot \frac{A_0}{\beta}\frac{\pi}{l} \cdot e^{-2\pi\beta\frac{y}{l}} \tag{8}$$

Equation 8 yields that the pressure raise due to the casing contour is primarily dependent on:

- the distance y from the casing
- the amplitude A_0 and l ($A_0 << l$)
- the Prandtl factor $\beta = \sqrt{1 - M_\infty^2}$, thus the meridional Mach number of the turbomachinery flow

Finally, equation 8 can be combined with equation 4 in order to find the pressure raise which leads to critical conditions $S_{crit} = \sqrt{2}$ for a clearance vortex with a given initial swirl ratio S_{ci}. A detailed derivation and analysis of the latter has been published in Kröger [5].

INFLUENCE OF THE CASING CONTOUR ON THE CLEARANCE VORTEX AND LOSS MECHANISMS

For the discussion of the impact of the casing contour on the clearance vortex, a simple example is used which has already been presented by Kröger et al. [1]. The optimized casing and blade tip shape, shown in Figure 4, was the result of an automated optimization process of the casing above a typical stage gas compressor rotor leading to a performance improvement of about 0.35% stage efficiency. Of course, the clearance height t did not change during the optimization process.

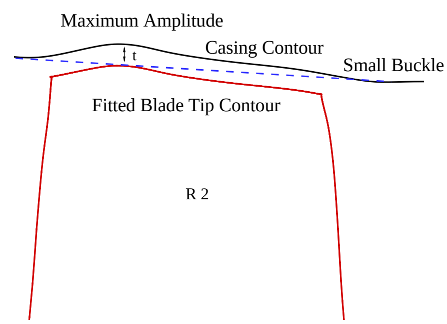

FIGURE 4. SHAPE OF CASING AND ROTOR TIP SECTION [1]

Resuming the aerodynamic effects of the optimized configuration in comparison to the baseline configuration which are both pictured in figure 5 in terms of the vorticity magnitude it was observed that:

- The clearance vortex core area is increased and the angle between the blade suction surface and the clearance vortex core line is higher
- The losses of the clearance vortex with the casing contour are higher up to about 30% chord and lower in the last 70% chord

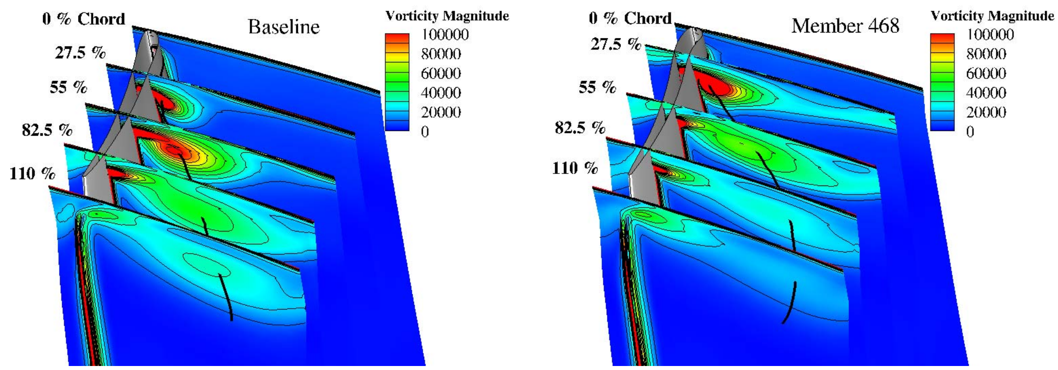

FIGURE 5. DEVELOPMENT OF THE CLEARANCE VORTICES, BASELINE LEFT, CONFIGURATION WITH SIMPLE CASING CONTOUR (MEMBER 468) RIGHT, ISOLINES OF VORTICITY MAGNITUDE ($|\nabla \times \vec{V}|$)[1]

– The overall losses of the optimized configuration are smaller

These aerodynamic effects can be explained by the simplified clearance vortex model and the knowledge about pressure distribution close to the optimized casing shape. Since the clearance vortex is in super-critical state ($S_{ci} \simeq 0.27 < \sqrt{2}$), the increasing static pressure near the casing caused by the casing contour leads to an increased vortex core area and consequently to a lower rotating speed of the vortex (constant circulation, conservation of angular momentum). Being a the radius of the vortex core and Γ its circulation, the power of the viscous moment per length unit at radius a of the baseline configuration is [12]:

$$L_a = \frac{\eta \Gamma^2}{\pi a^2} \quad \text{with} \quad \Gamma = 2 \cdot a \cdot \pi \cdot u_\theta \tag{9}$$

Taking into account the velocity distribution of a Rankine vortex outside the core area at a radius $r > a$ the power of the viscous moment per length unit at radius r is [12]:

$$L_r = \frac{\eta \Gamma^2}{\pi r^2} \tag{10}$$

The difference between the power values per length unit is dissipated into heat, yielding:

$$\Delta L = \frac{\eta \Gamma^2}{\pi} \left(\frac{1}{a^2} - \frac{1}{r^2}\right) \tag{11}$$

Hence the power of the viscous moment outside the vortex core is proportional to $\frac{1}{a^2}$ for a constant circulation Γ. As the static pressure increase of the casing contour does not conduct work on the vortex the circulation Γ is retained but the vortex dissipates less energy per length unit after the vortex core expansion. However, during the expansion of the vortex core more energy is dissipated to accomplish the transition to a higher vortex core radius. Figure 6 renders schematically the velocity distribution of a Rankine vortex before and after a vortex core expansion. Therefore, higher dissipation can be observed in the early phase of the vortex development, whereas lower losses occur after the vortex core expansion.

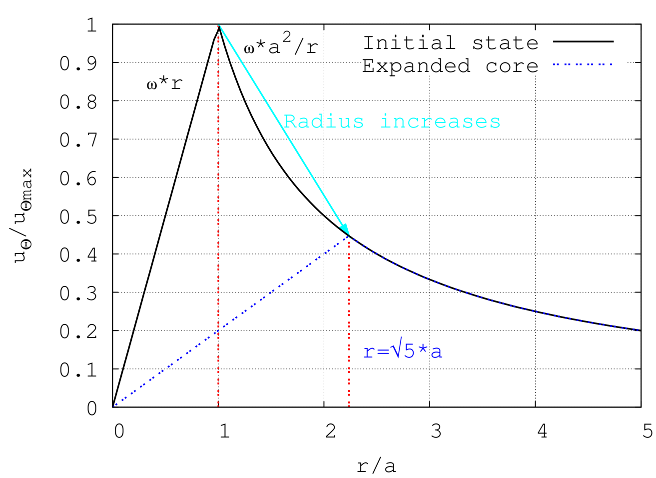

FIGURE 6. VELOCITY DISTRIBUTION OF A RANKINE VORTEX BEFORE AND AFTER A CORE EXPANSION

A secondary effect arises from the interaction of the clearance flow and the clearance vortex. This interaction is completely three dimensional and highly complex. The power balance requires a continuous energy supply for a stable vortex being realized by the clearance flow. However, the momentum which can be added from the clearance flow to the clearance vortex is inversely proportional to the angle between the clearance flow and the vortex core trajectory. Thus, in case of a bigger angle, by trend less energy is supplied to the clearance vortex and the vortex dissipates earlier.

A final comment is to be made on the interaction between the main flow and the clearance vortex. If the clearance vortex core state is shifted close to critical conditions ($S_{crit} = \sqrt{2}$) a very large expansion of the vortex core and vortex instability can be observed resulting in high losses due to the mixing process of the disrupted vortex and the main flow.

INDUSTRIAL APPLICATION: OPTIMIZED CASING CONTOUR AND BLADE TIP AIRFOIL SECTION

As first application the result of a joined optimization of the casing contour and the blade tip is presented. The CFD model of the optimization configuration consisted of two typical high pressure gas turbine compressor stages provided by the Siemens AG, Fossil Power Generation Division. The characteristic geometrical parameters of the rotor to be optimized are a small blade height, a small aspect ratio and a relatively large tip clearance gap. The Reynolds number based on the chord length at the blade tip and the inflow velocity is about $4.5 \cdot 10^6$. The CFD model which has been already presented in detail in the work of Kröger et al. [1] is shown in figure 7. Both stators are cantilevered.

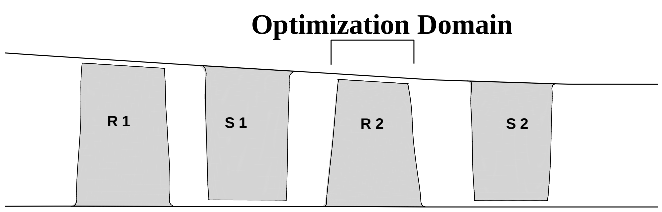

FIGURE 7. CFD MODEL FOR OPTIMIZATION [1]

The first stage was used to ensure correct inflow conditions for the second stage and to avoid a direct influence of the boundary conditions on the optimization result. The casing above rotor 2 and the last 15% of the blade height were subject to the optimization process. A single passage steady state CFD model was used for this purpose. Mesh resolution was about 400.000 cells per blade passage and for the second stage about 800.000 per blade passage resulting in a total of ca. 2.4 million mesh cells. The optimization only included the ADP at nominal rotating speed.

The fitness functions quantitatively define the objectives of an optimization. The isentropic stage efficiency of stage 2 was taken as first optimization objective. Since an optimization of the blade in the upper 15% span changes the radial work load of the blade and consequently the pitchwise averaged total pressure distribution at the rotor exit plane, the second fitness function was designed to retain the stage matching and to reduce the endwall blockage. As presented in figure 8, an ideal pitchwise averaged total pressure distribution was defined at the rotor exit plane (red solid line). The integrated absolute difference between the ideal distribution and the real distribution (black solid line) was taken as second objective function, referred to as “Pressure Deficit Area”.

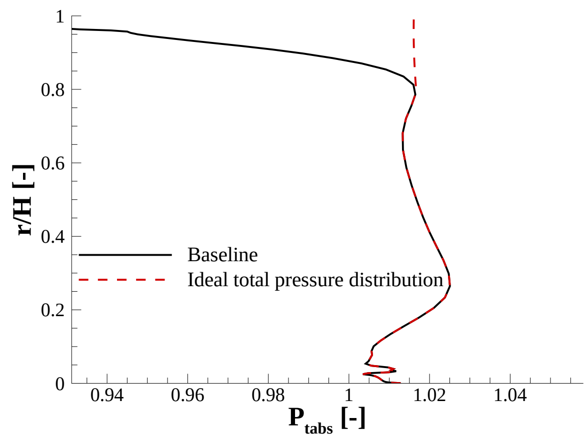

FIGURE 8. DEFINITION OF THE IDEAL ABSOLUTE TOTAL PRESSURE DISTRIBUTION AT THE ROTOR 2 EXIT PLANE

Geometrical parameters for airfoil section optimization
suction surface using a B-Spline description
thickness distribution for pressure surface parametrization
position of maximum thickness
stagger angle
leading and trailing edge angles
forward sweep

TABLE 1. GEOMETRICAL PARAMETERS FOR AIRFOIL SECTION OPTIMIZATION

A total of 38 variable geometrical parameters were used for the optimization, 12 for the definition of the new casing shape,

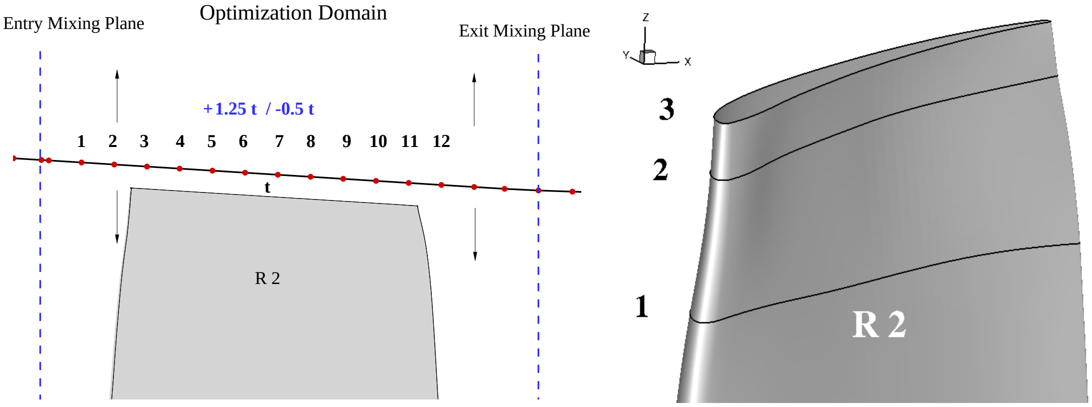

FIGURE 9. FREE VARIABLES ON OUTER ANNULUS LINE (LEFT FRAME) AND POSITION OF ADJUSTABLE CONSTRUCTION AIRFOIL SECTIONS (RIGHT FRAME) [5]

3 for the stacking line and 23 for the blade shape modification by means of three construction airfoils. The free geometrical parameters defining the casing shape and the radial position of the construction airfoils are shown in figure 9. Each point could be shifted independently in radial direction with a limit of +1.25/-0.5 clearance heights t. The blade tip shape followed the casing contour in radial direction so that the tip clearance height was kept constant during the optimization process. An analysis of the transient thermal behavior of the rotor and the casing has been performed to eliminate any possibility of a blade rubbing event at all operating conditions. Without going into detail of the airfoil section parametrization the free optimization parameters affected mainly the common generalized airfoil section meta parameters given in table 1. In order to retain the stage matching the degrees of freedom of construction airfoil section one were limited to small changes of the leading edge, trailing edge and stagger angle.

The automated optimization process was based on the DLR evolutionary algorithm AutoOpti [2, 13, 14] and the DLR flow solver TRACE [15, 16]. Furthermore, the optimization was to a great extend supported by Kriging and Neural network surrogate models to accelerate the very stable but slow evolutionary algorithm AutoOpti. Overall, more than 1800 converged CFD calculations (geometries) have been processed during the optimization process leading to a broad variety of combined efficiency-blockage optimized geometries. Finally, it is the choice of the designer to select the best geometry to fulfill the design requirements.

OPTIMIZATION RESULTS

For the discussion of the optimization results one representative geometry has been selected, namely Member 420. The new annulus line geometry of Member 420 is pictured in figure 10. The wavy casing shape is basically dominated by two local maxima at about 25% and 60% axial chord and a deep local minimum between them. Additionally, the first wave is characterized by a shape with a produced upswing. A small second local minimum can be seen behind the second wave. The ratio between the amplitude of imaginary sinusoidal wave A_z with wavelength l and the clearance height t yields ($\frac{A_z}{l} \simeq 0.05$):

$$\frac{A_z}{t} \simeq 0.4 \tag{12}$$

A comparison of the airfoil sections of the optimized and the baseline configuration about one clearance height below the blade tip is presented in figure 11. The optimized airfoil section provides a much higher camber in the last 50% of the chord length implying a rear loaded airfoil design. Especially the trailing edge metal angle was notably decreased and the leading edge shape is slightly asymmetrical.

A three dimensional view of the blade tip section of Member 420 is rendered in figure 12. The characteristics of the new casing shape and the increased camber of the airfoil sections at the blade tip is reflected in this rather unusual blade shape. However, the optimized geometry is able to gain numerically a significant isentropic stage efficiency improvement of about 0.8% at ADP conditions (convergence uncertainty: ~0.02%). Additionally, the endwall blockage in terms of the second objective function was notably decreased in the upper 20% of the duct height. Figure 13 shows the comparison of the pitchwise averaged absolute total pressure distributions of Member 420 and the baseline geometry at the rotor 2 exit plane. Whereas the total pressure distribution in the lower 80% of the relative duct height are mostly identical, the large pressure drop in the last 20% relative duct height is considerably reduced by the optimized casing and blade shape.

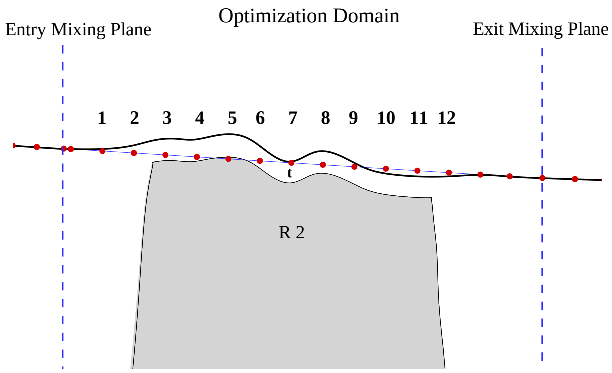

FIGURE 10. MERIDIONAL CASING AND ROTOR 2 SHAPE OF THE OPTIMIZED GEOMETRY MEMBER 420 [5]

Consequently, as a direct effect of lower losses and a higher flow turning, more work is done in the outer airfoil sections close to the blade tip.

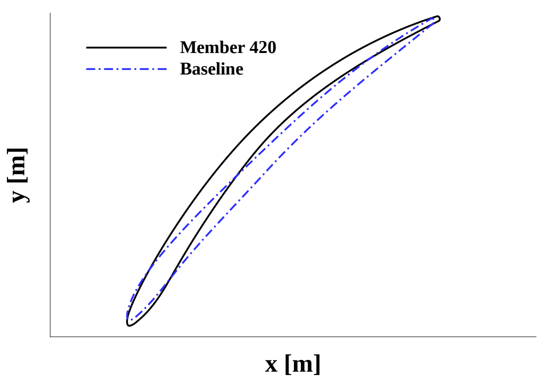

FIGURE 11. COMPARISON OF THE AIRFOIL SECTION DESIGN ABOUT ONE CLEARANCE HEIGHT BELOW THE BLADE TIP [5]

The remarkable improvement in isentropic stage efficiency of about 0.8% is generated in both, the rotor 2 and the following stator 2. The difference in isentropic rotor efficiency between the baseline configuration and Member 420 is depicted in the upper frame of figure 14 as radial distribution over the relative massflow (black solid line). Furthermore, the figure includes the same analysis for the geometry with the simple casing contour without any airfoil section manipulation (Member 468, solid blue line), see figure 4 [1]. In the upper 20% relative duct height

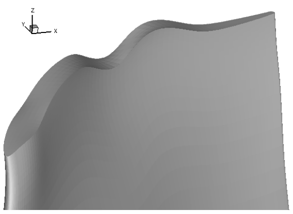

FIGURE 12. 3D VIEW OF THE OPTIMIZED BLADE TIP [5]

Member 420 gains up to 5% isentropic efficiency in comparison to the baseline design and still up to 3% in comparison to the simple casing contour design.

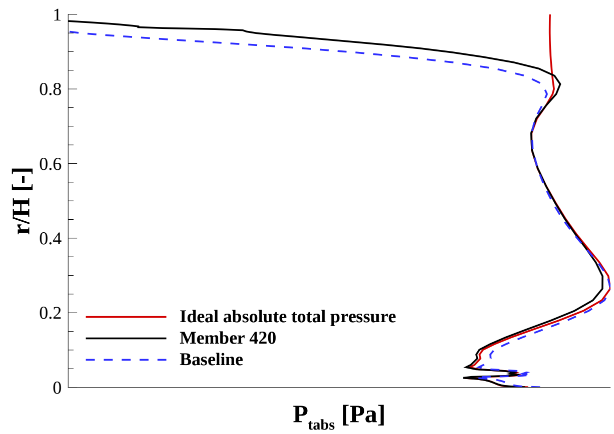

FIGURE 13. PITCHWISE AVERAGED ABSOLUTE TOTAL PRESSURE DISTRIBUTIONS AT THE EXIT PLANE OF ROTOR 2 OF THE OPTIMIZED CONFIGURATION (BLACK SOLID LINE) AND THE BASELINE CONFIGURATION (BLUE DASHED LINE)

A similar analysis is presented in the lower frame of figure 14 for the stator 2 loss coefficient. Because of the improved inflow conditions, Member 420 provides lower losses than the baseline design and Member 468 in the upper 20% duct height. However, the enhanced work in the rotor blade tip area of Member 420 yields a change of the radial load distribution and hence, the hub section airfoils of the stator 2 suffer from higher incidence and thus from higher losses. On the other hand, a slight modification of the stator hub airfoils section could be used to even the stator losses in the lower 10% of the relative massflow. A cross check at Siemens Energy with the commercial flow solver CFX showed very similar results.

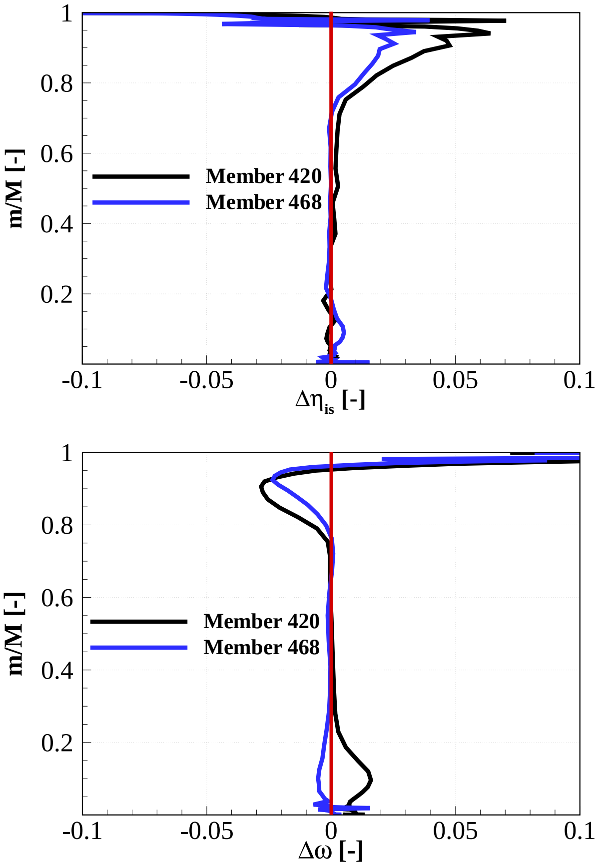

FIGURE 14. EFFICIENCY IMPROVEMENT OVER RELATIVE MASSFLOW (m/M) OF ROTOR 2 (UPPER FRAME) AND LOSS REDUCTION OVER RELATIVE MASSFLOW (m/M) OF STATOR 2 (LOWER FRAME) OF MEMBER 420 (BLACK SOLID LINE) AND THE SIMPLE CASING CONTOUR (MEMBER 468, BLUE SOLID LINE) VERSUS THE BASELINE DESIGN AT ADP CONDITIONS [5]

To conclude the aerodynamic analysis figure 15 presents a comparison of the relevant flow phenomena in the 3D flow field between the baseline (left frames) and Member 420 (right frames). The top frames show the development of the clearance flow via the absolute rotation of the flow field. The bottom frames picture the partial derivative of the static pressure in axial direction $\frac{\partial p}{\partial x}$ on a z-constant slice close to the blade tip. In good agreement to the analytic model and to the configuration with simple casing contour a higher rotation of the flow field and thus higher dissipation losses can be observed at the x-constant slice at 27.5% chord of Member 420. However, the clearance vortex of Member 420 detaches quickly with a high angle from the blade suction surface and dissipates.

The slice at 55% chord already shows much lower levels of flow field rotation. Whereas the flow field of the baseline design is dominated by one stable clearance vortex, a second smaller clearance vortex is formed in the optimized design. The second clearance vortex of Member 420 suffers from the same effects as the first one due to the second casing wave. It detaches quickly from the blade suction surfaces and dissipates. The illustrations of the partial derivative of the static pressure in axial direction reveal even more details. The baseline design is completely dominated by the accelerating and decelerating shear layers of the clearance vortex whilst the first clearance vortex core of the optimized design is enlarged leading to a low rotational speed of the clearance vortex and hence to low shear layer gradients. Furthermore, the formation of the second clearance vortex can be also detected in the axial pressure gradient of Member 420.

Aside from the isentropic efficiency at design point conditions the operating range of the optimized design is of primary interest, especially for the gas turbine peak load operation mode. Figure 16 displays the 100% rotating speed line of the second stage at different operating conditions. The ADP static back pressure at the stator 2 outlet plane was taken as reference to throttle the full configuration numerically (see figure 7) to -1.25%, +1.85, +3,7% and +4,9% back pressure, respectively. The efficiency improvement even increases numerically to about 1% stage efficiency running the compressor in dethrottled mode. At higher stage loading, the efficiency advantage of the optimized design gradually vanishes to the last numerically stable operating point (+4.9% reference back pressure). Additionally, the optimized configuration shows numerically a small massflow rate increase due to the reduced blockage and a overall speed line widening implying an enhanced operating range.

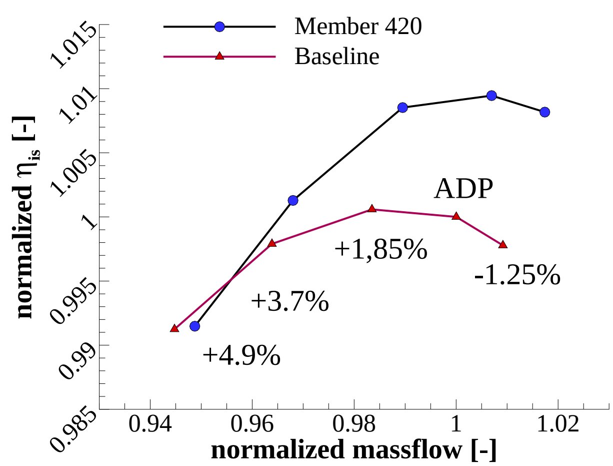

FIGURE 16. STAGE 2, 100% ROTATING SPEED LINE

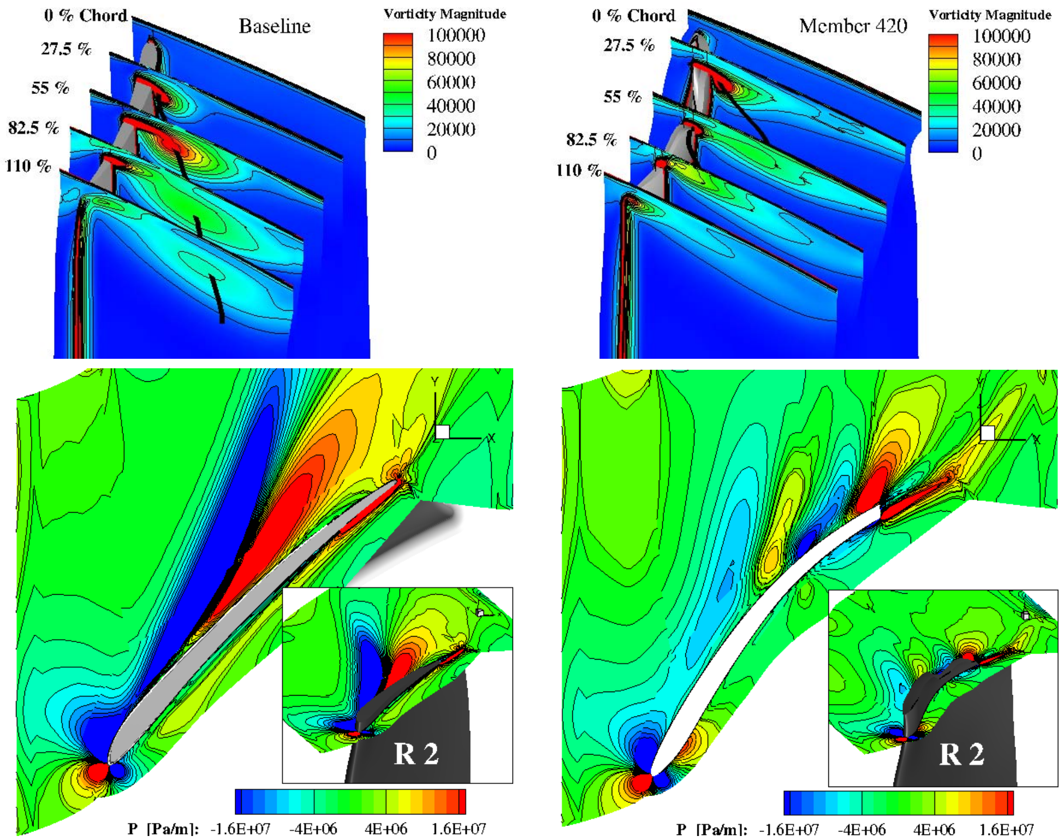

FIGURE 15. DEVELOPMENT OF THE CLEARANCE VORTICES, ISOLINES OF VORTICITY MAGNITUDE (TOP FRAMES) AND $\frac{\partial p}{\partial x}$-Z-CONSTANT SLICES CLOSE TO THE BLADE TIP (BOTTOM FRAMES), BASELINE LEFT, OPTIMIZED CONFIGURATION RIGHT (MEMBER 420)

WHOLE COMPRESSOR/ENGINE APPLICATION

A whole compressor CFD model has been used to validate the transfer rules of the casing contour and airfoil tip modifications. The individual gain in efficiency of each modified stage and the impact on the stage matching of the rear stages were the two most important aspects of this CFD evaluation. The CFD analysis should verify by a detailed analysis of the flow in the tip clearance region that the combination of the used objective functions is a reasonable approach for an optimization of a single airfoil in a multi-stage compressor environment. Further, the overall efficiency improvement for a typical compressor configuration could be estimated based on these CFD results.

Based on the transfer rules that have been developed for the blade tip and the casing contour the six last stages of a typical Siemens GT compressor have been modified. The compressor that has been chosen for the CFD evaluation is a first prototype version of the 13 stage SGT5-8000H compressor with HPA airfoils [17, 18] for the 8 high pressure stages (see figure 17). The compressor has an inlet mass flow of >800 kg/s at a pressure ratio of 19.2 and provides an IGV and three variable vanes for improved part load efficiency.

A typical distribution of the radial clearances increasing from the first stage towards the last stages was applied for this analysis. In the real engine the actual hot running clearances depend mainly on the thermal behavior of the specific mechanical design of GT rotor and casing. The casing contouring and the tip sections have been modified depending on the individual radial clearance, the stagger and camber angle of each blade. The geometry of the casing contour has to be defined carefully because there are significant relative axial and radial shifts of the rotor (blade tip) and the casing while start up and shut down of the gas turbine. In the current study the shape of the casing contour was restricted such that under all operating conditions contact of blade tips and casing is avoided.

A grid of 24.5 M nodes with about 900 k nodes per passage has been used for the whole compressor CFD prediction. The grid resolution was the same that has been used for the automated optimization of the blade tip region. The grid size with high resolution in the blade tip region allows that all relevant details of the tip clearance flow are resolved. The CFD model includes the

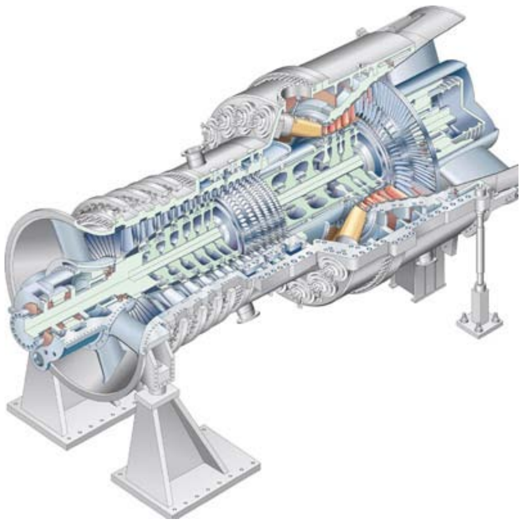

FIGURE 17. SIEMENS SGT5-8000H

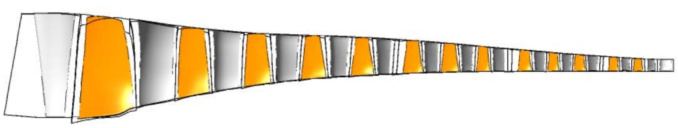

FIGURE 18. WHOLE COMPRESSOR CFD MODEL

airfoil fillets, the part chord clearances at shrouded variable vanes and the bleed flow extractions. TRACE has been used for the analysis of the whole compressor. Figure 18 shows the baseline flowpath geometry of the single passage CFD model.

The gain in efficiency compared to the baseline of the rear stages is shown in figure 19. The gain in efficiency mainly depends on the actual clearance size, therefore the gain is lower in the middle stages. Additional sensitivity studies that have been performed for different designs of the optimized last stage showed a strong correlation between tip clearance size and the gain in efficiency compared to the baseline design, but even with tight clearances of less than 1% span height an increase in efficiency was achieved with the optimized geometry [5]. For the last stage that has been optimized a 1.2 % increase in efficiency is computed. This is even higher than the gain predicted within the optimization (the 2 stage model), because also the core flow region of blade 13 benefits from the improved inflow conditions with less blockage generated by the upstream stages.

The detailed examination of the CFD results confirmed, that the objective functions that have been used are suitable for an isolated optimization of a single stage of a multi stage compressor. The reduction of endwall blockage due to casing contouring and a appropriate change of the loading at the blade tip have improved the overall stage matching. The inflow conditions to the downstream vanes are significantly improved

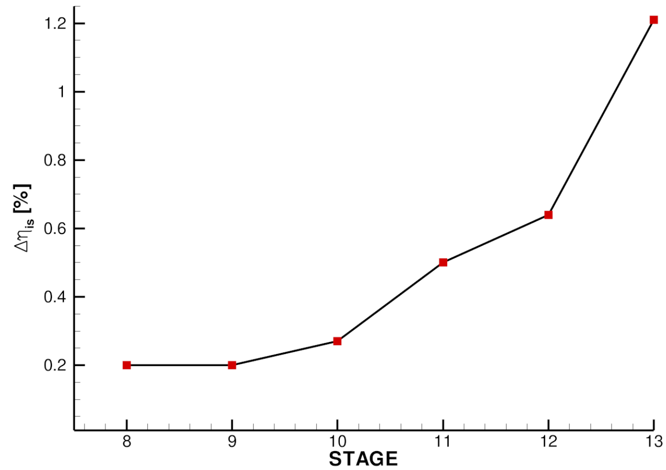

FIGURE 19. STAGE EFFICIENCY IMPROVEMENT

in the off-design region and the radial flow distribution is more even. Especially the rear stages with relatively large radial clearances benefit from the modification in the tip region. Fig 20 shows the difference of the pitchwise averaged meridional Mach number distribution between optimized and baseline design for the stages 10 to 12.

The CFD predicts an overall efficiency increase of 0.3%, which is a significant improvement and for increased clearances as they could be expected for a compressor with higher pressure ratio the benefit would be even higher.

Siemens Energy is currently working on the development of a next generation 3D design for the rear stages of the gas turbine compressor partially funded by the BMWi within the COORETEC-FlexComp program. In addition to the blade tip modification an optimization of the blade root sections as well as the stacking line will be included. Besides the peak efficiency at design point the improved operating range will be a main objective. A succeeding AG-turbo project on the automated optimization of the endwall sections of blades and vanes will be started in January 2011.

CONCLUSION AND OUTLOOK

The present work shows that the tip clearances losses and endwall blockage of subsonic compressor rotors with relatively large clearance heights can be effectively reduced by means of an axisymmetric contouring of the outer annulus line and adapted optimized blade tip shape. The aerodynamic effects causing this performance improvement have been explained via an analytic approach of a two-dimensional compressible subsonic flow along a sinusoidal wall. The clearance vortex was approximated as Rankine vortex.

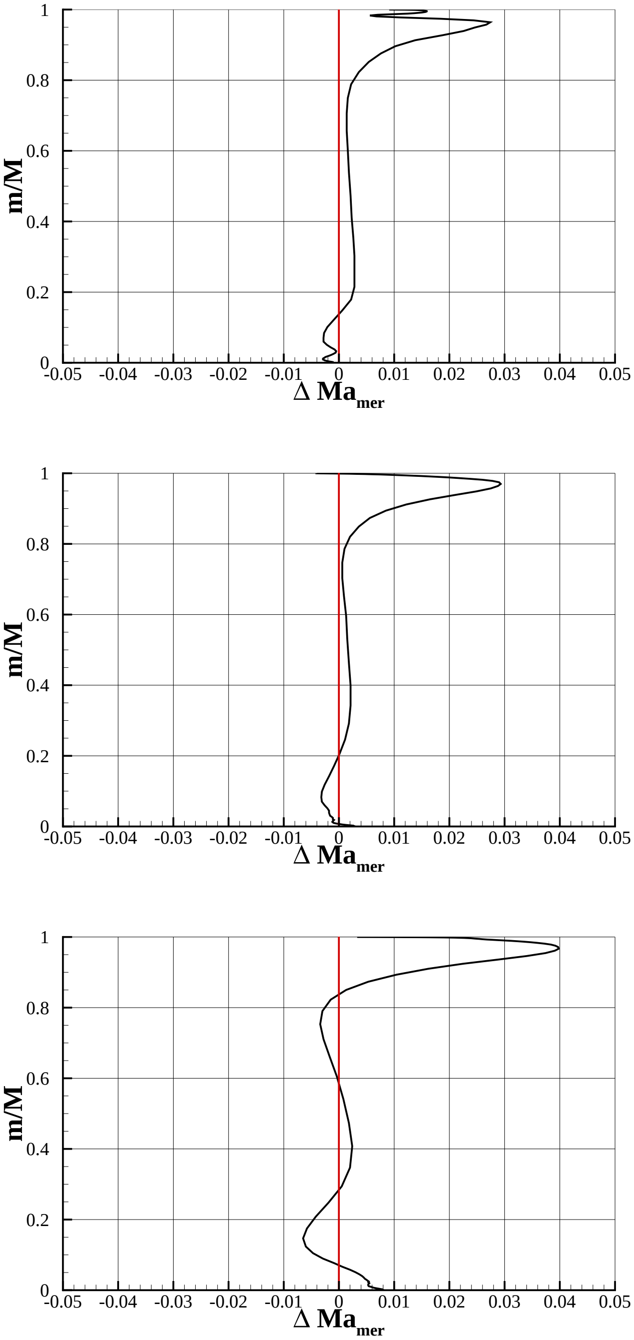

FIGURE 20. DELTA IN MERIDIONAL MACH NUMBER AT STAGE 10 (TOP FRAME), STAGE 11 (MID FRAME) AND STAGE 12 (BOTTOM FRAME) OVER RELATIVE MASSFLOW (m/M)

Due to the wavy casing shape the static pressure close to the endwall is increased forcing the clearance vortex core to expand. The influence of the casing shape on the clearance vortex primarily depends on the distance between the clearance vortex and the casing, the meridional Mach number of the turbomachinery flow and the amplitude of the casing contour. A simplified consideration of the dissipated viscous energy per length unit confirms previous CFD results. In comparison to the baseline configuration the viscous losses per length are increased whilst the clearance vortex core is widened but a drop of the losses per length unit is achieved after the expansion process resulting altogether in an advantageous design.

An automated optimization of the outer annulus line and the blade tip section of a typical high pressure stage compressor rotor at design point conditions is presented as industrial application. During the optimization process, the basic evolutionary algorithm was largely supported by use of Neural network and Kriging surrogate models. A remarkable stage efficiency improvement of about 0.8% was achieved. Furthermore, the endwall blockage in the rotor tip area was notably reduced leading to a higher meridional velocity at the blade tip and to a small change in the radial massflow distribution. The downstream stator benefits from the improved inflow conditions at the blade tip but provides a slightly higher level of losses at the blade hub due to the change in the radial massflow distribution. The analysis of the off-design behavior showed an improved performance over the full operating range including a broader speed line characteristic. A cross validation at Siemens Energy with the flow solver CFX showed nearly identical results.

Finally, a CFD model of the first prototype version of the SGT5-8000H compressor was used to validate the transfer rules of the casing contour and the blade tip modifications. Based on these transfer rules the optimized blade tip and casing shape was applied to the last six stages of the whole compressor model. The CFD predicts a significant increase of the isentropic compressor efficiency of 0.3 % as well as a performance improvement for every modified stage ranging from 0.2% at stage 8 to 1.2% at stage 13. In doing so, in particular stage 13 profits from the improved inflow conditions generated upstream. Aside from the performance enhancement an improved stage matching is observed due to the consecutive endwall blockage reduction.

Aiming to enhance the overall compressor efficiency further projects could focus on axisymmetric endwall contours for cantilevered stator blades. Additionally, the sensitivity of the performance improvement concerning the axial position of the rotor blade could be investigated.

ACKNOWLEDGMENTS

The investigations were partially conducted as part of the joint research programme COORETEC-turbo in the frame of AG Turbo. The work was partially supported by the Bundesministerium für Wirtschaft und Technologie (BMWi) as per resolution of the German Federal Parliament under grant number 0327715A. The authors gratefully acknowledge AG Turbo and Siemens AG for their support and permission to publish this paper. The responsibility for the content lies solely with its authors.

References

[1] G. Kröger, C. Cornelius, and E. Nicke. Rotor Casing Contouring in High Pressure Stages of Heavy Duty Gas Turbine Compressors With Large Tip Clearance Heights. *ASME Turbo Expo 2009, Orlando, USA GT2009-59626*, 2009.

[2] G. Kröger, C. Voß, and E. Nicke. Axisymmetric Casing Optimization for Transonic Compressor Rotors. *ISROMAC 13 2010, Honolulu, USA, ISROMAC-2010-20010*, 2010.

[3] E.M. Greitzer, C.S. Tan, and M.B. Graf. *Internal flow: concepts and applications*. Cambridge Univ Pr, 2004.

[4] G. Kröger, C. Cornelius, and E. Nicke. *Beeinflussung der Spaltströmung durch Optimierung der Geometrie im Schaufelspitzenbereich*. AG-Turbo Abschlussbericht, COORETEC-TURBO Teilvorhaben 1.2.1 des Verbundprojektes CO2-Reduktions-Technologien, September 2009. Förderkennzeichen 0327715 A.

[5] G Kröger. *Beeinflussung von Rotorspaltströmungen durch rotationssymmetrische Gehäusekonturen*. PhD thesis, Ruhr-Universität Bochum, ISSN 1434-8454, ISRN DLR-FB-2010-33, 2010.

[6] J.A. Storer and N.A. Cumpsty. Tip leakage flow in axial compressors. *Journal of Turbomachinery*, 113:252, 1991.

[7] S. Kang and C. Hirsch. Experimental Study on the Three-Dimensional Flow Within a Compressor Cascade With Tip Clearance: Part II—The Tip Leakage Vortex. *Journal of Turbomachinery*, 115:444, 1993.

[8] M.K. Smart, I.M. Kalkhoran, and S. Popovic. Some aspects of streamwise vortex behavior during oblique shock wave/vortex interaction. *Shock Waves*, 8(4):243–255, 1998.

[9] D.L. Darmofal, R. Khan, E.M. Greitzer, and C.S. Tan. Vortex core behaviour in confined and unconfined geometries: a quasi-one-dimensional model. *Journal of Fluid Mechanics*, 449:61–84, 2001.

[10] K. Burg, S. Viriyabhun, and J. Zierep. Die Überschallströmung längs einer welligen Wand mit grader Gegenwand. *Acta Mechanica*, 16:271–278, 1973.

[11] J. Zierep. *Theoretische Gasdynamik*. Braun Karlsruhe, 1991.

[12] J.H. Spurk and N. Aksel. *Strömungslehre: Einführung in die Theorie der Strömungen*. Springer, 2006.

[13] C. Voß, M. Aulich, B. Kaplan, and E. Nicke. Automated multiobjective optimization in axial compressor blade design. *ASME Turbo Expo 2006, Barcelona, Spain GT2006-90420*, 2006.

[14] U. Siller, C. Voß, and E. Nicke. Automated Multidisciplinary Optimization of a Transonic Axial Compressor. *47 th AIAA Aerospace Sciences Meeting, Orlando, USA, AIAA-2009-0863*, 2009.

[15] G. Ashcroft, K. Heitkamp, and E. Kügeler. High-order accurate implicit runge-kutta schemes for the simulation of unsteady flow phenomena in turbomachinery. *Proceedings of V European Conference on Computational Fluid Dynamics ECCOMAS CFD*, Lisbon, Portugal, 2010.

[16] K. Becker, K. Heitkamp, and E. Kügeler. Recent progress in a hybrid-grid cfd solver for turbomachinery flows. *Proceedings of V European Conference on Computational Fluid Dynamics ECCOMAS CFD*, Lisbon, Portugal, 2010.

[17] U. Köller, R. Mönig, B. Küsters, and H.A. Schreiber. Development of advanced compressor airfoils for heavy-duty gas turbines- Part I: Design and optimization. *Journal of Turbomachinery*, 122(3):397–405, 2000.

[18] B. Küsters, H.A. Schreiber, U. Köller, and R. Mönig. Development of advanced compressor airfoils for heavy-duty gas turbines: Part II: Experimental and theoretical analysis. Discussion. *Journal of turbomachinery*, 122(3):406–415, 2000.